Journal of Intelligent Manufacturing
https://doi.org/10.1007/s10845-021-01781-4

Gaussian-process based modeling and optimal control of melt-pool geometry in laser powder bed fusion

Yong Ren[1] · **Qian Wang**[1]

Received: 23 January 2021 / Accepted: 6 May 2021

Abstract
Studies have shown that melt-pool characteristics such as melt-pool size and shape are highly correlated with the formation of porosity and defects in parts built with the laser powder bed fusion (L-PBF) additive manufacturing (AM) processes. Hence, optimizing process parameters to maintain a constant melt-pool size during the build process could potentially improve the build quality of the final part. This paper considers the optimal control of laser power, while keeping other process parameters fixed, to achieve a constant melt-pool size during the laser scanning of a multi-track build under L-PBF. First, Gaussian process regression (GPR) is applied to model the dynamic evolution of the melt-pool size as a function of laser power and thermal history, which are defined as the input features of the GPR model. Then a constrained finite-horizon optimal control problem is formulated, with a quadratic cost function defined to minimize the difference between the controlled melt-pool size and its reference value. A projected gradient descent algorithm is applied to compute the optimal sequence of laser power in the proposed control problem. The GPR modeling is demonstrated using simulated data sets, a mix of simulated and experimental data sets, or pure experimental data sets. Numerical verification of the control design of laser power is performed on a commercial AM software, Autodesk's Netfabb Simulation. Simulation results demonstrate the effectiveness of the proposed GPR modeling and model-based optimal control in regulating the melt-pool size during the scanning of multi-tracks using L-PBF.

Keywords Laser powder bed fusion · Gaussian process regression · Optimal control · Multi-track · Melt-pool geometry

Introduction

Additive manufacturing (AM) has significantly broadened the design space for fabrication of components with complex geometries in comparison to conventional manufacturing technologies (Jiang et al. 2021). Laser powder bed fusion (L-PBF) AM processes are one subcategory of metal AM processes for manufacturing complex parts with a high geometric resolution and robust mechanical properties, with wide applications in medical, aerospace, and automotive industries (Levy et al. 2003; Kruth et al. 2007).

There are many process parameters that could affect the quality of build (Druzgalski et al. 2020), among which the most commonly modulated parameters include laser power, scan speed, and laser beam diameter. Especially, laser power is often considered as the most convenient knob to control the melt-pool dimensions. If the laser power (and the resulting energy density) is too low, it will result in a small melt-pool and lack of fusion. On the other hand, if the laser power is too high, it will result in overmelting and keyholing. The latter is observed more frequently at laser turnarounds during scanning a multi-hatch build with switching laser travel directions, where the returning end of the track gets heated repeatedly, indicating the need of online control of laser power during the build process. Studies have shown that the melt-pool size is highly correlated with the development of porosity and part defects (Dilip et al. 2017; Kumar et al. 2019; Ning et al. 2020). Hence, in order to reduce or eliminate either lack-of-fusion or keyhole-induced porosity to achieve a better build quality, one possible solution is to design a model-based laser power control to regulate the melt-pool size during the build process, which is the objective of this

✉ Qian Wang
quw6@psu.edu

Yong Ren
yzr51@psu.edu

[1] Department of Mechanical Engineering, The Pennsylvania State University, University Park, PA 16802, USA

Published online: 17 May 2021

paper. To achieve this objective, a model that can enable the model-based process control is needed.

One line of the existing literature on model-based control of process parameters for L-PBF AM relied on transfer-function models derived from system identification (Craeghs et al. 2010; Wang et al. 2019). For example, in Craeghs et al. (2010), transfer-function models were identified based on the experimental data on laser power and the resulting melt-pool surface area measured with photodiode signals. In Wang et al. (2019), a first-order transfer function was identified to model the dynamics from the laser power to melt-pool width, where simulated data from finite-element-analysis (FEA) models were used for the system identification. Analytical lumped-parameter models, in the form of ordinary differential equations, were also developed and used to derive the control of laser power to regulate the melt-pool size in the build process of multi-tracks (Wang 2019; Wang et al. 2020). Finite difference equations on the isotherm positions were defined and used to design a linear state feedback controller for laser power to regulate the melt-pool size (Devesse et al. 2014, 2016) or to design a feed-forward controller to regulate the melt-pool width (Dillkötter and Mönnigmann 2019). A computation framework was established in Druzgalski et al. (2020) for part-scale process optimization under L-PBF, where a feature extraction was first used to identify scan vectors that require process parameter adaptation and then a simulation-based feed-forward control was applied to optimize the complex geometries.

Note that transfer functions are limited to modeling linear systems. The lumped-parameter models reviewed above are restricted by over-simplified assumptions on temperature-independent material properties, linear heat equations, and many others. Simulation-based part-scale process optimization and the resulting feed-forward control impose a high computational cost and require running on the high-performance computing platforms (Druzgalski et al. 2020). On the other hand, machine learning (ML) could be integrated with process physics to develop physics-informed ML models, offering a complementary modeling approach that might achieve a higher modeling accuracy than the transfer-function models or lumped-parameter models. In addition, ML models, once trained, would enable faster predictions on the testing samples than FEA.

Machine learning has been applied in many aspects of AM research. A large number of studies focused on leveraging ML's powerful capacity in image recognition for classification of build quality and defect detection, e.g., applying ML to the melt-pool, layer, or part images either in an ad hoc fashion or during the build process (Gobert et al. 2018; Yuan et al. 2018; Yang et al. 2019; Scime and Beuth 2018, 2019; Gaikwad et al. 2020; Aminzadeh and Kurfess 2019; Zhang et al. 2018), where various ML models such as support vector machine, (deep) neural networks, and multifractal analysis were developed. Machine learning has also been applied to the design for AM, material design, characterization of microstructure, and many other aspects of AM research and industry practice, see the recent review papers (Razvi et al. 2019; Meng et al. 2020) and references therein.

What is the next step after part defects are detected from the melt-pool, layer, or part images? One natural question would be how to control the laser process parameters to improve the build quality, which requires the development of a process model that characterizes how process parameters would affect the build quality. Applying ML techniques to the modeling of AM processes is still limited. For a directed energy deposition (DED) system, a back propagation network with adaptive learning rate and a least-square support vector machine were trained to map the process parameters to the depositing height by Lu et al. (2010). Recurrent neural networks were developed to predict the thermal history and temperature field (Mozaffar et al. 2018; Ren et al. 2020) for DED processes. For selective laser sintering, neural networks and genetic algorithms were applied to search the optimal layer thickness, hatch spacing, laser power, speed, and work surrounding temperature that can yield the minimum shrinkage ratio (Rong-Ji et al. 2009). Back propagation neural networks were developed to model the spreading process (Zhang et al. 2017). A random forest network model was applied to use morphology of pore distribution to predict fraction porosity, median pore diameter and pore spacing in L-PBF (Kappes et al. 2018).

Several studies also developed ML models to predict melt-pool size, surface area, or an individual dimension (e.g., melt-pool width or depth) for L-PBF processes, but restricted to *single-track builds* (Yang et al. 2018; Tapia et al. 2018; Gaikwad et al. 2020; Meng and Zhang 2020). A dynamic meta-modeling method using kriging covariance matrices was applied to predict the melt-pool width and then genetic algorithms were applied to optimize the process parameters (Yang et al. 2018). In Tapia et al. (2018), Gaussian processes were used to construct a surrogate response surface model to predict the melt-pool depth as a function of process parameters consisting of the laser power and laser scanning speed. The Gaussian-process based model was trained and validated on experimental data of single-track deposits of 316L stainless steel. In addition, the study by Tapia et al. (2018) also demonstrated that the Gaussian-process based surrogate model can be trained using simulated data sets from the powder-scale simulation model (Khairallah et al. 2016), and the resulting model can then serve as an approximation of the high-fidelity simulation to identify process windows keeping the melt pool away from the keyhole mode. A similar Gaussian process-based model was developed in Meng and Zhang (2020) to predict the remelted depth of single tracks of stainless steel as a function of laser power and scan speed, using simulated and experi-

mental data. A sequential-decision-analysis neural network model was developed in Gaikwad et al. (2020), where measurement data from pyrometer and high-speed video camera were used to train the proposed neural networks to predict the melt-pool mean width (and the associated standard deviation) as well as the continuity of single-tracks as a function of laser power and speed. However, as acknowledged in Tapia et al. (2018), the afore-mentioned ML models for single-hatch builds only considered the melt-pools in steady state and were not applicable to multi-hatch parts, as the models cannot accommodate the scan pattern and the resulting thermal history during the build process for multi-hatch builds.

In Ren et al. (2019), for multi-tracks built with L-PBF, a two-level ML modeling architecture was proposed, where the lower-level model was trained to learn the pre-scan temperature (a proxy for thermal history) and the upper-level model was trained to predict the melt-pool size using the output of the lower-level and process conditions. However, similar to the afore-mentioned ML models on single-tracks (Yang et al. 2018; Tapia et al. 2018; Gaikwad et al. 2020; Meng and Zhang 2020), the ML model in Ren et al. (2019), although applicable to multi-tracks, still suffered from the limitation that the ML model was built to learn a static process map from the process parameters to an output of interest, where "static" here means no dynamics during the build process being accounted. As a result, these afore-mentioned ML models were often used with genetic algorithms to identify the optimal but constant values for process parameters. However, what are the optimal values for process parameters may change during the build process. For example, if one layer becomes too hot, the next layer may need to be scanned at a lower energy density. For multi-track scanning where the laser switches the scan direction, the area around laser turnarounds often gets overheated and thus requires reducing the laser power, i.e., varying laser process parameters are needed to respond to the dynamic evolution of melt-pool size or dimension along the laser scanning during the build process.

This paper investigates the use of Gaussian process regression (GPR) to model the dynamic evolution of melt-pool size, with the objective of designing GPR model-based control of laser power to regulate the melt-pool size during the build process to improve the build quality.

GPR defines a normal distribution over functions, and has been widely used in modeling unknown physical processes and dynamics in many areas (Rasmussen and Williams 2006; Beckers et al. 2019). First, this paper trains the GPR to model the discrete dynamic equation that governs the evolution of a melt-pool geometric variable. Appropriate input features are identified based on physical-domain knowledge of the melt-pool dynamics by including the thermal history to enable the derived model applicable to multi-hatch parts. Melt-pool volume is used as the representative geometric variable in this study, but the modeling approach is applicable to any melt-pool geometric variables such as the melt-pool dimensions, surface area, or cross-sectional area. In addition to the contribution to modeling, a GPR-model based optimal control is designed to regulate the melt-pool volume during the build process, where a gradient (steepest descent) based controller on laser power is derived to optimize a cost function that minimizes the difference of the controlled melt-pool volume and its reference value.

In this paper, a commercial FEA software on the thermo-mechanical simulation of metal AM processes, Autodesk's Netfabb Simulation, is used to generate simulated data sets. There is increasing interest in developing ML models to learn from FEA simulations such that the resulting ML models could be potentially used to replace the FEA models when rapid predictions are needed (Baturynska et al. 2018). FEA models for computing the melt-pool size accounted for heat conduction in a solid, but not fluid mechanics or vaporization that is critical in characterizing and prediction of keyhole-induced porosity. Nevertheless, as long as the laser power (or energy density) is controlled appropriately to maintain the melt-pool in the regime where no keyholing will appear, it is reasonable to consider that the assumption of heat conduction holds. In this paper, the proposed GPR modeling is demonstrated using pure simulated data sets (Sect. 5.1), a mix of simulated and experimental data sets, or pure experimental data sets (Sect. 6). Numerical verification of the GPR-based optimal control is performed on the Netfabb Simulation as well. Preliminary results of this paper were presented at the 2020 ASME Dynamic Systems and Control Conference (Ren and Wang 2020). In this paper, significant new results have been added in terms of both methodologies and datasets. Newly added methods include: (1) computing standard deviation of the GPR predicted mean on melt-pool size by the covariance function of GPR; and (2) a new method for training over a mixed set of simulated and experimental data and subsequent prediction. Newly added data sets include: (1) experimental data sets and the corresponding training/prediction results; and (2) numerical verification of the control design on Netfabb for 6-track cases, whereas only verification of 2-track cases was presented in the conference paper. All figures and Tables on results in Sect. 5 and Sect. 6 of this paper are new (not published in the conference paper).

Preliminaries on Gaussian process regression

Gaussian process regression (GPR) models can be interpreted as defining a distribution over functions, which are assumed to be random. The predictions from a GPR model take the form of a predictive distribution, which is completely specified by its mean function and covariance function.

Consider a set of n noisy observations $\mathcal{O} = \{(\mathbf{x}_i, y_i)|y_i = f(\mathbf{x}_i)+v, i = 1, \ldots, n\}$, drawing random functions from the training data, where $\mathbf{x}_i$ denotes an input vector of dimension d and y_i denotes a scalar output or target value. The noise v is assumed to follow a zero-mean Gaussian distribution with variance σ_n^2, i.e., $v \sim \mathcal{N}(0, \sigma_n^2)$. Assume that the random function $f(\mathbf{x})$ has a zero mean with covariance function $k(\mathbf{x}, \mathbf{x}') = cov(f(\mathbf{x}), f(\mathbf{x}'))$. The covariance function is also referred to as the kernel function of a GPR model, which is often chosen based on the applications. A commonly used squared exponential kernel function is defined as

$$k(\mathbf{x}, \mathbf{x}') = \sigma_f^2 e^{-\frac{1}{2}(\mathbf{x}-\mathbf{x}')^T \sum^{-1}(\mathbf{x}-\mathbf{x}')} \tag{1}$$

where $\sum = diag([\sigma_{x_1}^2 \ldots \sigma_{x_d}^2])$, and $\{\sigma_f, \sigma_{x_1}, \ldots, \sigma_{x_d}\}$ is referred to as the set of hyperparameters of the GPR model.

Let X denote the design matrix that aggregates the column-vector inputs $\mathbf{x}_i$ and let $\mathbf{y}$ denote the vector of all target values y_i, $i = 1, \ldots, n$. Further let $K(X, X)$ denote the $n \times n$ matrix of the covariances evaluated at all pairs of $\mathbf{x}_i$. Then the covariance on the noisy observations becomes $cov(y, y') = k(\mathbf{x}, \mathbf{x}') + \sigma_n^2 \delta_{yy'}$, where $\delta_{yy'}$ denotes a Kronecker delta which equals one if $y = y'$ and zero otherwise. Consequently, the covariance matrix on the noisy observation pairs becomes $cov(\mathbf{y}) = K(\mathbf{y}, \mathbf{y}) = K(X, X) + \sigma_n^2 \mathbf{I}$.

If there are n_* testing data points, let $K(X, X_*)$ denote the $n \times n_*$ matrix of the covariances of all pairs of training and testing points. Further define $K(X_*, X)$ and $K(X_*, X_*)$ accordingly. Then the prediction of the GPR on the testing locations (X_*) conditioned on the training data $(X, \mathbf{y})$ satisfies the following (Rasmussen and Williams 2006):

$$\mathbf{f}_*|X, \mathbf{y}, X_* \sim \mathcal{N}(\widehat{\mathbf{f}}_*, cov(\mathbf{f}_*)) \tag{2}$$

where the predicted mean function of the testing data is given by

$$\widehat{\mathbf{f}}_* = K(X_*, X)[K(X, X) + \sigma_n^2 \mathbf{I}]^{-1} \mathbf{y} \tag{3}$$

and the predicted covariance function of the testing data is given by

$$cov(\mathbf{f}_*) = K(X_*, X_*) - K(X_*, X) \cdot [K(X, X) + \sigma_n^2 \mathbf{I}]^{-1} \cdot K(X, X_*) \tag{4}$$

Essentially the trained GPR model enables the prediction of the mean function of a given testing location and also provides the confidence intervals (variance) of the predicted mean function, quantifying the uncertainty bound.

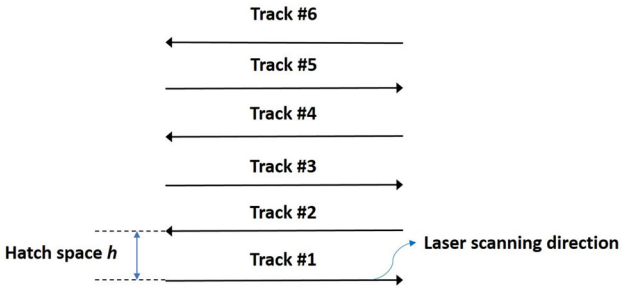

Fig. 1 Case study of a multi-track, single-layer part, where the laser switches the scan direction from track to track. All tracks have the same track length and hatch spacing

Modeling

This paper considers a multi-track as an illustrative example for the proposed GPR modeling and optimal control design. As shown in Fig. 1, the multi-track, single-layer part has a constant track length and an equal hatch spacing; the laser scans from track to track with a switching direction.

Gaussian process model on melt-pool dynamics

This section first introduces the general functional form that governs the dynamic evolution of the melt-pool geometric variables. Melt-pool volume is considered as the representative geometric variable in this study. In addition, consider that laser power is the single varying process parameter, with a constant laser scan speed and other process parameters fixed.

For each track i $(i = 1, 2, \ldots)$ in a multi-track build, let $s = 0, 1, \ldots, N.$ denote the discretized sequence of laser-travelled distance from the start of the track i, along the laser scanning direction, till the end of the track. Consider a step size of Δs for the discretized distance sequence and let L denote the track length, then $N\Delta s = L$. Inspired by our prior lumped-parameter model on the dynamics of melt-pool volume (Wang 2019; Wang et al. 2020), it is proposed that, for track i, the dynamic evolution of melt-pool volume with respect to the space coordinate s is governed by a nonlinear system $f(\cdot)$ defined as follows:

$$V(s+1) = f(V(s), Q(s); T_{init}(s)), \quad s = 0, \ldots, N-1 \tag{5}$$

where a superscript i denoting track i for all variables is omitted here for notation simplicity; $V(s)$ denotes the melt-pool volume at distance s, $Q(s)$ denotes the laser power applied at s, and $T_{init}(s)$ denotes the initial (or pre-scan) temperature of the selected-to-scan point at s before laser hits it (Wang et al. 2020, 2021) (see Appendix A for further details).

Remark 1 The authors' prior lumped-parameter model (Wang 2019; Wang et al. 2020) derived the explicit mathematical expression of the nonlinear function $f(\cdot)$ in terms

of the melt-pool volume, varying laser power, any given constant laser scanning speed, and the initial temperature, based on the melt-pool energy balance. The lumped-parameter model on melt-pool dynamics indicates that during the scanning of a multi-track, the variation of melt-pool volume along s not only depends on the laser power but also depends on thermal accumulation from the scanning of all past tracks, represented by the initial temperature $T_{init}(s)$. As shown in Appendix A, when the laser scans the first track ($i = 1$), the initial temperature $T_{init}(s)$ equals to the ambient temperature T_a for all s. However, when $i > 1$, the computation of the initial temperature $T_{init}(s)$ accounts for the temperature contributions from all past tracks being scanned. Including the initial temperature $T_{init}(s)$ as one input feature in (5) makes the GPR model physics-informed.

Remark 2 It should be noted that the laser scan path (build plan) is not explicitly included as an input in the function $f(\cdot)$ since the computation of the initial temperature T_{init} in terms of temperature contributions from the past tracks has already taken into account the laser scan path, as well as the inter-hatch skywriting time and any additional dwell time (Wang et al. 2020).

In this paper, rather than deriving the nonlinear function $f(\cdot)$ in (5) explicitly based on first principles as in Wang (2019), Wang et al. (2020), which suffered from many simplifications and approximations, $f(\cdot)$ is learned by a Gaussian process regression model from data. For a given s, consider that the input-feature vector of the function $f(\cdot)$ consists of the melt-pool volume $V(s)$, laser power being applied $Q(s)$, and the initial temperature $T_{init}(s)$. Thus define $\boldsymbol{\xi}(s) \in \mathbb{R}^3_+$, with $\boldsymbol{\xi}(s) = [V(s), Q(s), T_{init}(s)]^T$, $s = 0, \ldots, N-1$. to denote the vector of input features for the function $f(\cdot)$. By applying a GPR on the nonlinear function $f(\boldsymbol{\xi})$, $f(\boldsymbol{\xi}) \sim \mathcal{GP}(\widehat{f}(\boldsymbol{\xi}), cov(\boldsymbol{\xi}))$, where $\widehat{f}(\boldsymbol{\xi})$ and $cov(\boldsymbol{\xi})$ denote the predicted mean function and covariance function of $f(\boldsymbol{\xi})$, respectively.

Furthermore, a multi-step prediction by the GPR using the recursive method is applied here to update the predicted mean of the nonlinear system $f(\cdot)$ in (5), i.e., the prediction of $V(s+1)$ ($\widehat{V}(s+1)$) depends on the predicted sequence $\widehat{V}(s)$, $\widehat{V}(s-1)$, ..., with only V_0 drawn from the measurement. Consequently, consider that the estimated melt-pool volume satisfies the following discretized system:

$$\widehat{V}(s+1) = \widehat{f}(\widehat{V}(s), Q(s); T_{init}(s)), \quad s = 0, \ldots, N-1 \quad (6)$$

where $\widehat{V}(s)$ denotes the predicted melt-pool volume at s, and $\widehat{f}(\cdot)$ represents the GPR predicted mean function of $f(\cdot)$. In this paper, only the predicted mean function $\widehat{f}(\boldsymbol{\xi})$ of the GPR model is considered in the recursive prediction used for control design. Noting that the nonlinear iteration of a Gaussian distribution does not ensure a Gaussian distribution anymore, the propagation of the entire Gaussian distribution for the recursive prediction and the subsequent control design might be pursued in the future work and are beyond the scope of this paper.

Recursive evaluation of GPR Prediction

The discrete melt-pool dynamic equation in (6) requires recursively predicting the melt-pool volume from the GPR model. Consider (3) and define $\mathbf{w} = [K(\mathbf{X}, \mathbf{X}) + \sigma_n^2 \mathbf{I}]^{-1}\mathbf{y}$, which is of dimension $n \times 1$ and computed in terms of the training data $\mathbf{X}$. By the covariance matrix of the noisy observations $K(\mathbf{y}, \mathbf{y}) = K(\mathbf{X}, \mathbf{X}) + \sigma_n^2 \mathbf{I}$, $\mathbf{w} = K^{-1}(\mathbf{y}, \mathbf{y})\mathbf{y}$. Note that σ_n^2 denotes the variance of the observation noise. When the simulated data sets are obtained from finite-element simulations, they can be considered to be noise free. Nevertheless, a small value of σ_n^2 should be assigned in order to ensure that $K(\mathbf{y}, \mathbf{y})$ is nonsingular and positive definite so that its inverse can be computed.

After $\mathbf{w}$ is computed using the training data, for each track, by following (3), the iteration of the GPR-predicted state variable (melt-pool volume) along the sequence of the discretized sampling steps in (6) is derived as follows:

$$\widehat{V}(1) = K(\boldsymbol{\xi}(0), \mathbf{X})\mathbf{w}, \quad (7)$$

$$\widehat{V}(2) = K(\widehat{\boldsymbol{\xi}}(1), \mathbf{X})\mathbf{w}, \quad (8)$$

$$\cdots$$

$$\widehat{V}(N) = K(\widehat{\boldsymbol{\xi}}_{N-1}, \mathbf{X})\mathbf{w}. \quad (9)$$

with

$$\boldsymbol{\xi}(0) = [V(0), Q(0), T_{init}(0)]^T,$$
$$\widehat{\boldsymbol{\xi}}(1) = [\widehat{V}(1), Q(1), T_{init}(1)]^T,$$
$$\cdots$$
$$\widehat{\boldsymbol{\xi}}(N-1) = [\widehat{V}(N-1), Q(N-1), T_{init}(N-1)]^T.$$

Note that $\boldsymbol{\xi}(0)$, $\widehat{\boldsymbol{\xi}}(1)$, ..., $\widehat{\boldsymbol{\xi}}(N-1)$ here correspond to the testing locations X_* in (3), with $n_* = 1$ that makes each $K(X_*, X) = K(\widehat{\boldsymbol{\xi}}(s), \mathbf{X})(s = 0, \ldots, N-1)$ a matrix of dimension $1 \times n$.

Consider a squared exponential covariance function as follows,

$$k(\boldsymbol{\xi}, \boldsymbol{\xi}') = \sigma_f^2 e^{-\frac{1}{2}[(\xi_1-\xi_1')^2/\sigma_{l1}^2 + (\xi_2-\xi_2')^2/\sigma_{l2}^2 + (\xi_3-\xi_3')^2/\sigma_{l3}^2]} \quad (10)$$

where the hyper-parameters include $\sigma_f, \sigma_{l1}, \sigma_{l2}, \sigma_{l3}$. Then the GPR predicted melt-pool states in (7) - (9) can be computed accordingly, and the explicit expressions in terms of the squared exponential covariance function are given in Appendix B.

Table 1 Process parameters and material properties used in simulation; *: constant thermal conductivity and thermal diffusivity are used in computing the initial temperatures in eq. (28) of Appendix A

Parameter	Value
Hatch space (mm)	0.1
Laser beam diameter (mm)	0.075
Laser scan speed (mm/s)	600
Dwell time (s)	2.0×10^{-4}
Laser absorption efficiency	0.4
Convection coefficient (W/mm^2K)	2.5×10^{-5}
Material density (kg/mm^3)	8.44×10^{-6}
Melting temperature (^oC)	1295
Latent heat of fusion (J/kg)	287000
Thermal conductivity* (W/mm K)	0.0258
Thermal diffusivity* (mm^2/s)	5.5488

Table 2 Temperature-dependent thermal conductivity and specific heat used in the Netfabb FEA simulations

T (°C)	Thermal conductivity k (W/mm K)	Specific heat C_p (J/kg K)
25	10.0e−3	405
200	12.5e−3	460
300	14.0e−3	480
400	15.0e−3	500
500	16.0e−3	525
600	18.0e−3	550
800	22.0e−3	600
900	24.0e−3	630
1000	25.0e−3	650
1200	25.5e−3	680
1290	102e−3	

Data acquisition for model training and testing

In this study, the proposed modeling is first demonstrated using simulated data sets, which are generated from Autodesk's Netfabb Simulation, a commercial finite-element software on thermal-mechanical analysis of metal AM systems. Later in the paper, Sec. 6 illustrates how the model training and validation can be performed using a mixed set of simulated and experimental data, or pure experimental data sets.

To generate the training data from Netfabb, the scanning of a 6-track of Inconel 625, as shown in Fig. 1, is simulated with a constant laser scan speed, $v = 600$ mm/s, and a constant laser power taking one of the five different levels: 100 W, 150 W, 200 W, 250 W, and 300 W. Each track has a track length of 10 mm. The multi tracks are built on top of a substrate of Inconel 625 with a dimension of 20.15 mm × 10.65 mm × 4.04 mm. Process parameter values used in the simulations are summarized in Table 1, where the hatch space denotes the distance between two adjacent tracks. The temperature-dependent material properties of Inconel 625 are given in Table 2.

Normalization of system variables

System variables are normalized before model training. Specifically, the input features and the target value are normalized into a range of 0-1 using their respective maximum and minimum values. For example, the laser power $Q(s)$ is normalized as follows:

$$\overline{Q}(s) = \frac{Q(s) - Q_{\min}}{Q_{\max} - Q_{\min}}, \forall s = 0, \ldots, N-1. \tag{11}$$

Table 3 Maximum and minimum values of the input features and target value used in normalization

Variable	Minimum	Maximum
$V(s)$ (mm^3)	0	0.0096
$Q(s)$ (W)	100	300
$T_{init}(s)$ (^oC)	25	1200

As a result, $\overline{Q}_{\min} = 0$ and $\overline{Q}_{\max} = 1$. The normalization procedure is similar for other input features and the target value, with their corresponding maximum and minimum values given in Table 3. For the sake of simple illustration, notations of the input features and the target value are abused by continuing to use the symbols $Q(s)$, $T_{init}(s)$, and $V(s)$ to represent their respective normalized variables in the remainder of the paper.

Optimal control of melt-pool geometry

Formulation of a constrained finite-horizon optimal control problem

As demonstrated in our prior work (Wang 2019; Wang et al. 2020), when there is only a single track, applying constant process parameters is sufficient to maintain the melt-pool volume to be constant except during the short transient time at the beginning of the track. However, when more than one track is built, the melt-pool size at laser turnarounds gets significantly larger as the returning end of the track gets heated repeatedly. As a result, the melt-pool size will not stay constant from track to track even under the constant process parameters, indicating that starting from the second track, process parameters need to be adjusted to regulate the melt-pool size during the build process.

This study considers the laser power to be the single control variable while maintaining other process parameters fixed. For each track i ($i > 1$) in the multi-track, the objective of the control design is to adjust the laser power such that the melt-pool volume remains at a constant reference value during the scanning of track i. Such control is applied in a track-by-track fashion. Also note that the laser power used in the L-PBF machine has a physical lower and upper bound. Hence, the optimal control problem for each track i ($i > 1$) can be formulated as follows (where the subscript i for all variables is omitted here for the sake of notational simplicity):

$$\min_{\{Q(s)\}_{s=0}^{N-1}} \quad J = \sum_{s=0}^{N-1} (\widehat{V}(s+1) - V_{ref})^2 \tag{12}$$

$$\text{s.t.} \quad \widehat{V}(s+1) = \widehat{f}(\widehat{\boldsymbol{\xi}}(s)) \tag{13}$$

$$Q_{min} \le Q(s) \le Q_{max} \tag{14}$$

$$\widehat{V}_0 = V_0 \tag{15}$$

where $\widehat{\boldsymbol{\xi}}(s) = [\widehat{V}(s),\, Q(s),\, T_{init}(s)]^T, s = 0, \ldots, N-1$; the quadratic cost function is defined in terms of the difference between the predicted melt-pool size and its reference value; $\{Q(s)\}_{s=0}^{N-1}$ denotes the sequence of the laser power values; Q_{min} and Q_{max} denote the minimum and maximum laser power allowed by the L-PBF machine; and V_0 denotes the initial melt-pool volume at $s = 0$. The equality constraint in (13) is non-convex since the Gaussian kernel is non-convex. Hence, the optimization problem is non-convex.

Optimal control with a projected gradient descent

Recall that the iteration of the GPR-predicted melt-pool volume along the sequence of the discretized sampling steps in (13) can be derived recursively by following (7) - (9). Also note that a squared exponential covariance function (10) is differentiable. To solve the optimal control problem in (12) - (15), a projected gradient descent method is applied to derive the update rule of the control sequence $Q(s), s = 0, \ldots, N-1$. Let $\mathbf{U}(k)$ denote the kth iteration of the control sequence, i.e.,

$$\mathbf{U}(k) = \begin{bmatrix} Q^{(k)}(0) & \cdots & Q^{(k)}(N-1) \end{bmatrix}^T \tag{16}$$

Then the iterative update rule of the control sequence is given as follows:

$$\mathbf{U}(k+1) = \Pi_{\mathcal{Q}} \Big\{ \mathbf{U}(k) - \eta \cdot \nabla_{\mathbf{U}} J \Big\} \tag{17}$$

where $\mathcal{Q}$ is the feasible domain of $\mathbf{U}$ such that its elements are subject to the box constraint in (14); η denotes the learning rate; and $\nabla_{\mathbf{U}} J$ denotes the gradient of the cost function, which can be derived in terms of the differentiation of the squared exponential kernel function. Without considering the box constraints on the normalized laser power, the gradient of the cost function in (12) is computed as follows:

$$\nabla_{\mathbf{U}} J = \frac{\partial J}{\partial \mathbf{U}} = 2\mathbf{D}\widetilde{\mathbf{V}} \tag{18}$$

where the $N \times N$ matrix $\mathbf{D}$ takes the following form

$$\mathbf{D} = \begin{bmatrix} \frac{\partial \widehat{V}(1)}{\partial Q(0)} & \frac{\partial \widehat{V}(2)}{\partial Q(0)} & \cdots & \frac{\partial \widehat{V}(N)}{\partial Q(0)} \\ 0 & \frac{\partial \widehat{V}(2)}{\partial Q(1)} & \cdots & \frac{\partial \widehat{V}(N)}{\partial Q(1)} \\ \vdots & \vdots & \ddots & \vdots \\ 0 & 0 & \cdots & \frac{\partial \widehat{V}(N)}{\partial Q(N-1)} \end{bmatrix}. \tag{19}$$

and

$$\widetilde{\mathbf{V}} = \begin{bmatrix} (\widehat{V}(1) - V_{ref}) & \cdots & (\widehat{V}(N) - V_{ref}) \end{bmatrix}^T \tag{20}$$

The off-diagonal elements in matrix $\mathbf{D}$ can be computed in terms of the chain rule, e.g., $\frac{\partial \widehat{V}(2)}{\partial Q(0)} = \frac{\partial \widehat{V}(2)}{\partial \widehat{V}(1)} \cdot \frac{\partial \widehat{V}(1)}{\partial Q(0)}$. Consequently, the nonzero elements in $\mathbf{D}$ can be computed iteratively in a certain order, e.g., from left to right for each row, and then from the top row to the bottom row, utilizing the explicit expressions of the estimated state $\widehat{V}(s+1)$ and its partial derivatives with respect to $\widehat{V}(s)$ or $Q(s)$, which are given in (30) - (32) of Appendix B.

Simulation results and discussions

Modeling performance

As described in Sect. 3.3, simulated data sets were generated by running Autodesk's Netfabb to simulate the scanning of 6 tracks with the track length $L = 10$ mm, under the laser scan speed of $v = 600$ mm/s and each of the five different levels of laser power (100 W, 150W, 200W, 250W, and 300W). Among the total of 8010 simulated data points, 200 data points were randomly selected as the training data, and the rest were used as the testing data. Further increasing the number of training data points did not show significant improvement in prediction performance on the testing samples. The hyperparameters of the GPR were initialized as $\sigma_{l1}^2 = \sigma_{l2}^2 = \sigma_{l3}^2 = \sigma_f^2 = 1$. The noise variance is set as $\sigma_n^2 = 1 \times 10^{-4}$. Then a gradient descent method with backtracking line search was performed to optimize the hyperparameters by minimizing the log-marginal likelihood loss function $\epsilon(\boldsymbol{\theta})$ [1] (Rasmussen and Williams 2006), where $\boldsymbol{\theta}$ denotes the vector of hyperparameters $\boldsymbol{\theta} = \{\sigma_f, \sigma_{l1}, \sigma_{l2}, \sigma_{l3}\}$. The resulting

[1] $\epsilon(\boldsymbol{\theta}) = -\frac{1}{2}\ln(|K(\mathbf{y},\mathbf{y})|) - \frac{1}{2}\mathbf{y}^T[K(\mathbf{y},\mathbf{y})]^{-1}\mathbf{y} - \frac{\mathcal{N}}{2}\ln(2\pi)$

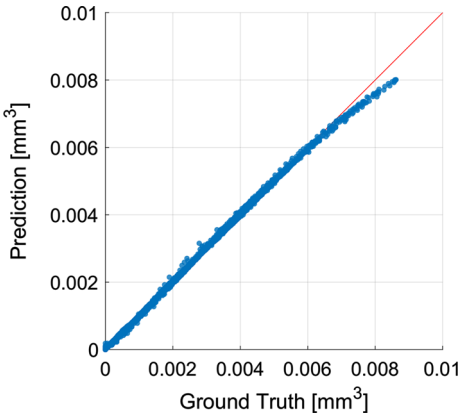

Fig. 2 Scatter plot of GPR's one-step prediction of melt-pool volumes on the testing samples versus Netfabb simulated melt-pool volumes (ground truth); L = 10 mm

hyperparameters obtained from the training are $\sigma_f^2 = 0.352$, $\sigma_{l1}^2 = 10.359$, $\sigma_{l2}^2 = 8.938$, and $\sigma_{l3}^2 = 2.171$.

One-step prediction

Evaluations were first conducted for one-step predictions on the testing data, i.e., computing $\widehat{\mathbf{y}}_\star = K(\mathbf{X}_\star, \mathbf{X})\mathbf{w}$, with $\mathbf{X}_\star$ denoting the design matrix of the testing data. Figure 2 shows the predicted melt-pool volumes versus the ground truth values, which demonstrates a good predictive performance of the GPR model on the testing data. The coefficient of determination (R^2) was computed to further assess the goodness of prediction, where $R^2 = 0.9992$. Since the testing samples were randomly selected, the results showed no over-fitting.

Recursive prediction

Note that solving the optimization problem in (12) requires recursively evaluating the state equation in (13). For the laser power of 250 W and the scan speed of 600 mm/s, Fig. 3a shows the recursive prediction of the melt-pool volumes versus the ground truth values along the (cumulative laser-travelled) distance for the six-track with the track length L = 10 mm, where the distance 0–10 mm is for track 1, ..., distance 50–60 mm is for track 6. The red solid line represents the recursively predicted mean for the melt-pool volume, and the shaded area represents two times standard deviation 2σ. The σ is computed from the GPR predicted variance of the recursively predicted mean, by applying (4) on the testing locations $\boldsymbol{\xi}(0), \widehat{\boldsymbol{\xi}}(1), \ldots, \widehat{\boldsymbol{\xi}}(N-1)$.

Without knowing V_0 of each track ahead of time, $V_0 = 0$ was used for each track in conducting the recursive predictions. Figure 3a shows that the recursive predictions of the GPR model have a reasonable agreement with the ground truth values for the first four tracks, but afterwards the prediction error grows with the increase of the track number, which is expected. The resulting root mean squared error (RMSE) between the recursively predicted melt-pool volume (red solid line) and the ground truth is 0.000266 mm^3, and the average error is 9.4%. The average error $e\%$ is defined as follows:

$$e\% = \frac{1}{n_s}\sum_{i=1}^{n_s}\frac{|\widehat{V}(i) - V_g(i)|}{V_g(i)} \times 100\% \tag{21}$$

where V_g denotes the ground truth value of the melt-pool volume, and n_s denotes the total number of samples. The accumulation of prediction errors could be potentially reduced by including more training data under various process conditions, or by improving accuracy in computing the initial temperatures.

The predictive performance of the GPR model is further evaluated on the 6-track with track length $L = 20$ mm under the same process conditions, as shown in Fig. 3b. Under the same sample step size Δs, the prediction for track length $L = 20$ mm takes double the iterations required in the recursive prediction for $L = 10$ mm for each track, i.e., $s = 0, \ldots, 2N-1$ in (6). The calculation of the initial temperature will need to be updated for $L = 20$ mm as well, but using the same analytical expressions. For $L = 20$ mm, the RMSE between the recursive prediction and the ground truth is 0.000197 mm^3 and the average error is 8%. It is worth pointing out that for a shorter track length, the effect of thermal buildup on the melt-pool size at laser turnarounds is more substantial. As a result, the gradient of melt-pool size with respect to the distance for $L = 10$ mm is larger than that for $L = 20$ mm and more prone to iterative modeling errors, which may explain why the recursive prediction for the case of $L = 20$ mm shows a reduced prediction error than the case of $L = 10$ mm in Fig. 3.

Control performance

For the first track, a constant laser power of 250 W (a nominal value used in the L-PBF) was applied. The steady-state value of the resulting melt-pool volume of the first track was then set as the the reference value to regulate the melt-pool volume for the second and subsequent tracks. Under the laser power of 250 W and the laser scan speed of 600 mm/s, the reference melt-pool volume $V_{ref} = 1.24 \times 10^{-3}$ mm^3. To obtain the laser power sequence for the second and subsequent tracks, the optimal control problem in (12) - (15) was solved. Specifically, the initial laser power sequence $\mathbf{U}(0)$ was set to be 250 W for all $Q_s(0)$, $s = 0, \ldots, N-1$. Then the projected gradient descent algorithm in (17) was applied to update $\mathbf{U}(k)$, where the learning rate η was determined through a backtracking line search in each iteration.

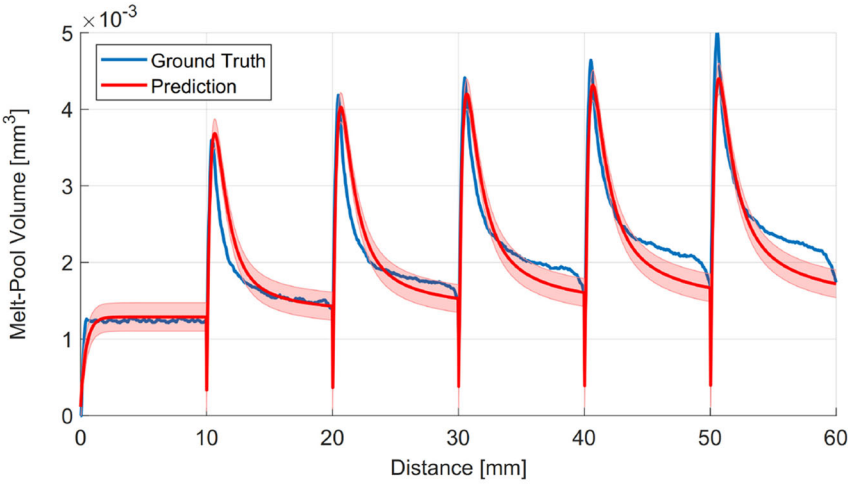

(a) Testing for $L = 10\ mm$

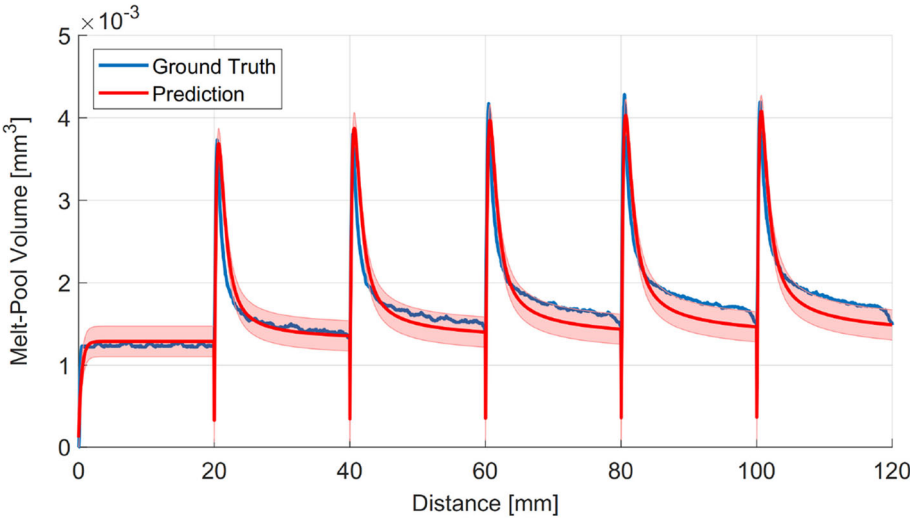

(b) Testing for $L = 20\ mm$

Fig. 3 Recursively predicted melt-pool volumes versus the ground-truth values for the six-track with respect to the (cumulative laser-travelled) distance, under the laser power of 250 W and scan speed of 600 mm/s. The red solid line represents the GPR predicted mean volume, and the shaded area represents two times the standard deviation (2σ), where σ is computed from the GPR predicted variance of the predicted mean. The ground-truth values are generated from Netfabb

Figure 4 shows the evolution of the cost function J with respect to the number of iterations in searching the optimal laser power sequence. The iteration was deemed to converge to a (local) minimum [2] when the improvement of the cost function at each successive iteration was less than 0.1%; the iteration would terminate at 50 if otherwise.

The control sequence for the laser power $(Q(s), s = 0, \ldots, N-1.)$ resulted at the end of the iterations for each of the second and subsequent tracks was then fed into the Netfabb to compute the corresponding melt-pool volumes, used for numerical evaluation of the control performance. Figure 5 shows the control performance for the six-track with $L =$ 10 mm under the laser scan speed of 600 mm/s. Specifically, Fig. 5a shows the controlled laser power trajectory versus the nominal laser power of 250 W (uncontrolled), and Fig. 5b shows the comparison among the uncontrolled melt-pool volume, the GPR prediction of melt-pool volume under the

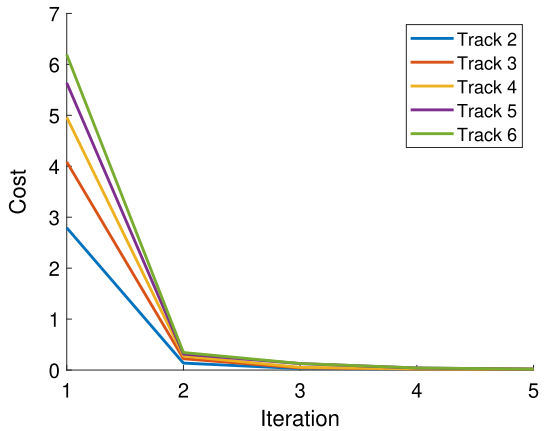

Fig. 4 Iteration of cost function during the gradient descent

[2] Noting that the optimization problem is nonconvex, the convergence to a global minimum is not guaranteed.

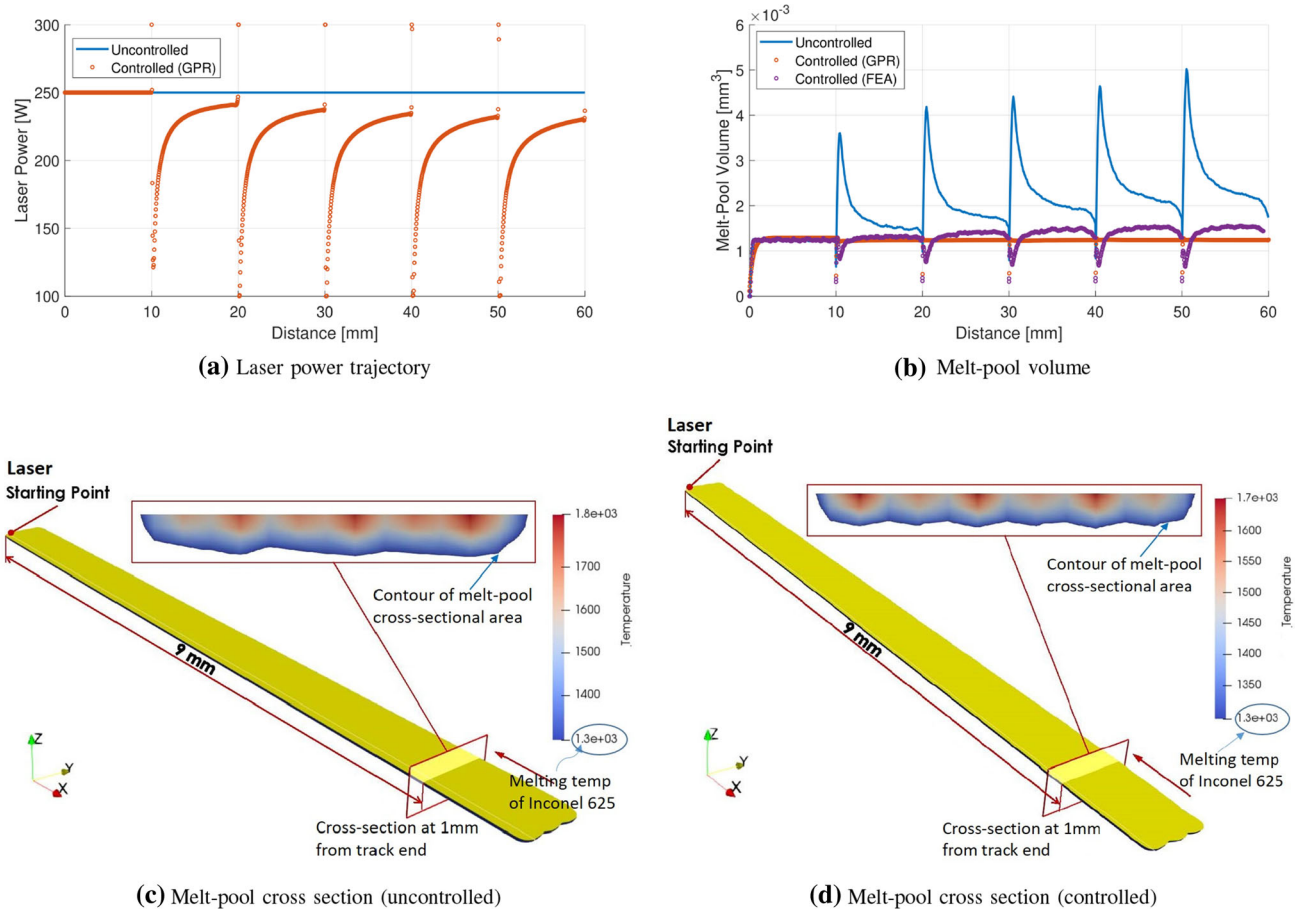

(a) Laser power trajectory

(b) Melt-pool volume

(c) Melt-pool cross section (uncontrolled)

(d) Melt-pool cross section (controlled)

Fig. 5 Control performance for a six-track with $L = 10$ mm under the laser scan speed of 600 mm/s

controlled laser power trajectory, and the Netfabb FEA simulation of melt-pool volume under the controlled laser power trajectory. Figure 5c and d show the FEA simulated melt-pool cross sections at 1 mm from the track end without and with control, respectively. With control, the melt-pool cross-section contours are much more evenly distributed, indicating relatively constant melt-pool cross-sectional areas, compared to the melt-pool cross-section contours without control. The control results of the six-track with $L = 20$ mm (under the same laser scan speed of 600 mm/s) are shown in Fig. 6.

Both Figs. 5 and 6 show that under the constant laser power of 250 W (uncontrolled), at the beginning of the second and each subsequent track (laser turnarounds), the melt-pool volume had a large overshoot due to heat accumulation. In contrast, such overshoot was almost flattened out under the controlled case by significantly reducing the laser power at the beginning of the second and each subsequent track. It was noted that the laser power jumped high at the first sample right after finishing each track to compensate for the cooling during the inter-hatch dwell (skywriting) time.

Table 4 summarizes the RMSE and error rate of the uncontrolled or controlled melt-pool volume with respect to its reference value. Compared to applying the nominal value (250 W) for laser power (uncontrolled), applying the optimal control for laser power (controlled FEA) has reduced the RMSE by $74\% - 78\%$ and $e\%$ by $73\% - 80\%$.

Computation cost

In this study, it took 54.8 seconds to compute the GPR based optimal control for the entire track 2–6 with 10 mm track length, and it took 145 seconds to compute the GPR based optimal control for the case of 20 mm track length, on a machine with Intel® Core i7-3632QM CPU, 2.20 GHz. In average, it took 11 seconds to compute the control for each 10 mm track and 29 seconds for each 20 mm track. As shown in Fig. 4, the gradient descent algorithm roughly converges within three iterations in average. A subsequent study was conducted to record the computation cost for running only three iterations for each track. The resulting computation time for each 10 mm track was less than 5 seconds, and was less than 13 seconds for each 20 mm track. Note that the proposed GPR control is applied track wise. For builds that require (inter-track) dwell time at the order of several sec-

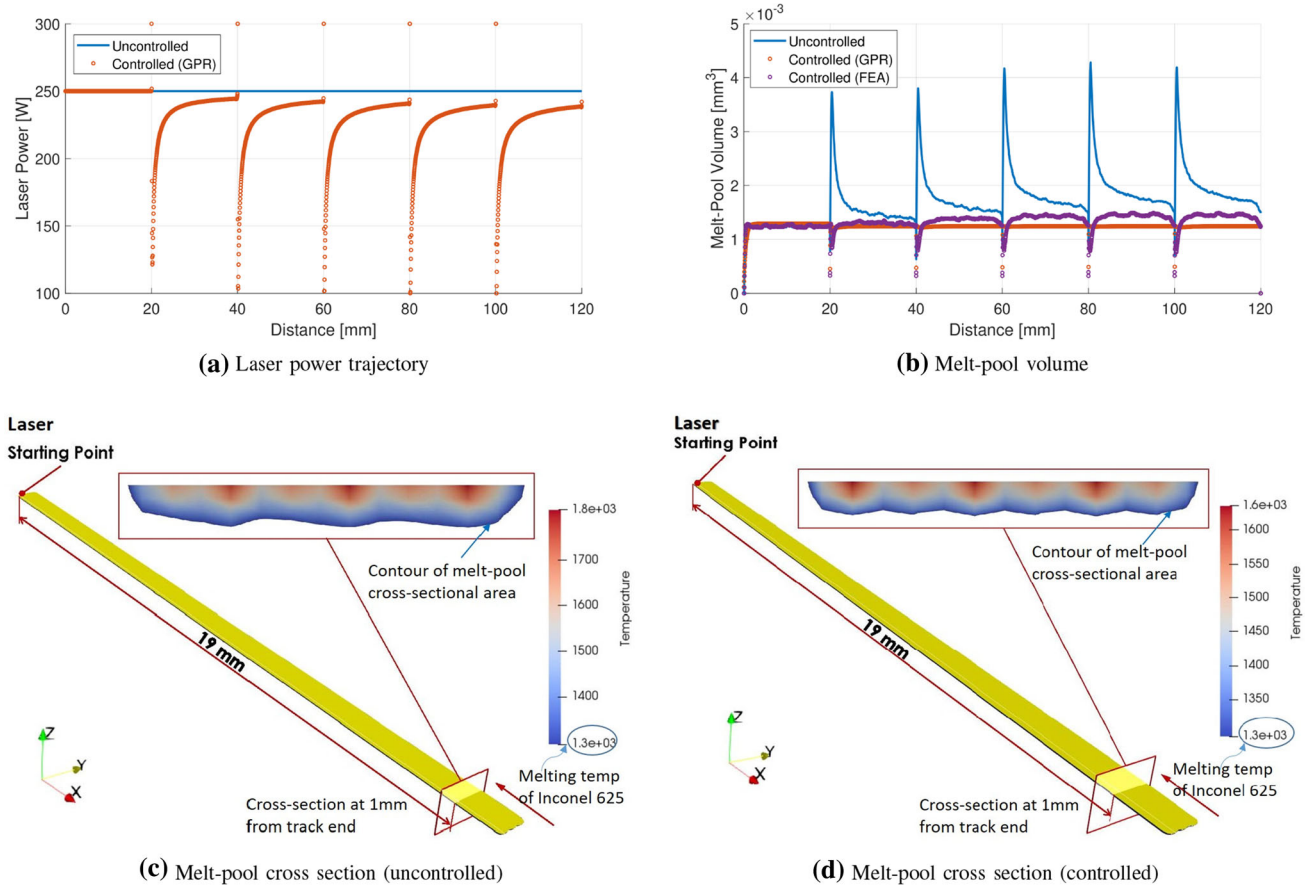

(a) Laser power trajectory

(b) Melt-pool volume

(c) Melt-pool cross section (uncontrolled)

(d) Melt-pool cross section (controlled)

Fig. 6 Control performance for a six-track with $L = 20$ mm under the laser scan speed of 600 mm/s

onds, one plausible way for implementation is to compute and load the control sequence during the (inter-track) dwell time, or during the inter-layer dwell time when it is applied to multi-layer builds. Another possible use of the proposed GPR control is to implement the control trajectory as a feed-forward control, in a similar way as the experimental study conducted in Wang et al. (2020).

Training over a mixed set of simulated and experimental data

Note that using simulated data sets from high-fidelity FEA models as training data could introduce bias and approximations originated from the governing physics and parameter values used in the FEA models. Hence, it is important to include experimental data for model training and validation. Considering that simulated data sets are often easy and cheap to obtain whereas the experimental data sets could be less accessible, this section proposes a method for model training using a mixed set of simulated and experimental data (where the number of available experimental data sets is much smaller than that of the simulated data sets) and conducts a numerical evaluation with respect to the relative confidence in the quality of the simulated versus experimental data.

Experimental data sets on melt-pool cross-sectional area

The simulated data sets generated from the Netfabb are on melt-pool volumes. However, it might be difficult to directly measure melt-pool volumes experimentally. This section utilizes the experimental measurements of the melt-pool cross-sectional areas obtained from our prior study (Wang et al. 2020). In Wang et al. (2020), a number of 1-track, 2-track, and 5-track bead-on-plate samples of Inconel 625, with track length of 10 mm, were built with a constant laser power of 250 W and a laser scan speed of 600 mm/s on an EOSINT M280 L-PBF system. As indicated in Ghosh et al. (2018), Heigel and Lane (2018), laser-powder interaction could cause significant errors in the measurements of melt-pool dimensions and thus the experimental study in Wang et al. (2020) chose to measure the melt-pool cross-sectional areas in the no-powder case for proof of concept. For each configuration (number of tracks in each sample),

Table 4 Evaluation of control performance: RMSE and error rate of uncontrolled and controlled melt-pool volume with respect to the reference value

	L = 10 mm		L = 20 mm	
	RMSE (mm^3)	$e\%$	RMSE (mm^3)	$e\%$
Uncontrolled (FEA)	10.96×10^{-4}	67.8	6.88×10^{-4}	40.3
Controlled (GPR)	8.17×10^{-5}	1.6	6.00×10^{-5}	1.1
Controlled (FEA)	2.36×10^{-4}	13.8	1.81×10^{-4}	11.0

four samples were repeated to account for experimental randomness. After the samples were built, cross-section cuts were performed at 1 mm from each end of the tracks, and then image processing was performed to measure the corresponding melt-pool cross-sectional areas (Wang et al. 2020). There are a total of 64 experimental data sets. The measured melt-pool cross-sectional areas with respect to the (cumulative laser-travelled) distance are plotted in Fig. 7. Note that it is very difficult, if not impossible, to take more cross-sections for the 10-mm track, as cross-sectioning and polishing result in a significant loss of material per cut, around 0.5–1.5 mm depending on the thickness of the cutting blade. This is where it is meaningful to consider model training using a mixed set of simulated and experimental data.

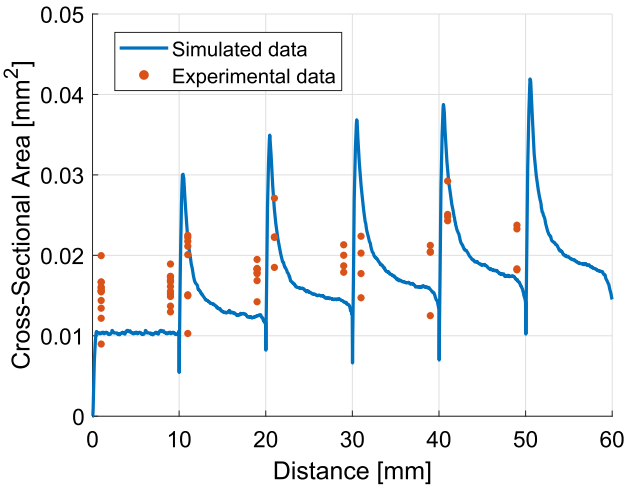

Fig. 7 A mixed set of simulated and experimental data on the melt-pool cross-sectional area with respect to the (cumulative laser-travelled) distance for a six-track; L = 10 mm, laser power = 250 W, and laser scan speed = 600 mm/s. Some experimental samples (partially) overlapped on each other

Conversion of simulated data sets

To be compatible with the experimental data on the melt-pool cross-sectional area for model training, the simulated data sets on melt-pool volumes for the six-track, with L = 10 mm under the laser power of 250 W and laser scan speed of 600 mm/s, are converted into melt-pool cross-sectional areas. Assuming that the melt-pool takes the shape of a half ellipsoid, the melt-pool area-to-volume ratio can be calculated as:

$$\gamma = \frac{A}{V} = \frac{3}{2l} \tag{22}$$

where l denotes the melt-pool length. Then the ratio γ is searched by solving the following minimization problem:

$$\gamma_* = \underset{\gamma}{\text{argmin}} \|\gamma \mathbf{V}_{sim} - \mathbf{A}_{exp}\|_2^2 \tag{23}$$

where $\|\cdot\|_2$ denotes the 2-norm; $\mathbf{V}_{sim}$ denotes the column vector of simulated melt-pool volumes and $\mathbf{A}_{exp}$ denotes the column vector of experimentally measured melt-pool cross-sectional areas, where the respective elements of $\mathbf{V}_{sim}$ and $\mathbf{A}_{exp}$ at the same row correspond to the same (cumulative laser-travelled) distance, i.e., same location in the track. Using the afore-mentioned simulated and experimental data sets (L = 10 mm, laser power = 250 W, scan speed = 600 mm/s), the melt-pool area-to-volume ratio is obtained as $\gamma_* = 8.3527\ m^{-1}$, by which the simulated data sets on the melt-pool volume are converted to the melt-pool cross-sectional area, as shown in Fig. 7.

Training and prediction

For GPR model training using a mix of simulated and experimental data sets, define a log-marginal likelihood loss function ϵ_α as a convex combination of the loss function ϵ_{exp} in terms of the experimental data sets $\mathcal{D}_{exp}$ and ϵ_{sim} in terms of the simulated data sets $\mathcal{D}_{sim}$, i.e.,

$$\epsilon_\alpha(\boldsymbol{\theta}) = \alpha\epsilon_{exp}(\boldsymbol{\theta}) + (1-\alpha)\epsilon_{sim}(\boldsymbol{\theta}) \tag{24}$$

where $\alpha \in [0, 1]$, and $\boldsymbol{\theta}$ denotes the vector of hyperparameters with $\boldsymbol{\theta} = \{\sigma_f, \sigma_{l1}, \sigma_{l2}, \sigma_{l3}\}$. The weight α reflects the confidence in the quality of the experimental data sets versus that of the simulated data sets, towards model training. For a given α, the optimized hyperparameters $\boldsymbol{\theta}^*$ are obtained by minimizing the weighted log-marginal likelihood function $\epsilon_\alpha(\boldsymbol{\theta})$.

It is assumed that the predictions on the testing samples follow a distribution that is a convex combination of the predictive Gaussian distributions from the experimental and simulated data sets. Then, the one-step predictions at testing samples $\mathbf{X}_*$ are computed as the convex combination of the predictions $\widehat{\mathbf{y}}_{exp}$ based on the experimental training data and

the predictions $\widehat{\mathbf{y}}_{sim}$ based on the simulated training data:

$$\widehat{\mathbf{y}} = \alpha\widehat{\mathbf{y}}_{exp} + (1-\alpha)\widehat{\mathbf{y}}_{sim} \tag{25}$$

where $\widehat{\mathbf{y}}_{exp} = K(\mathbf{X}_*, \mathbf{X}_{exp})\mathbf{w}_{exp}$, $\mathbf{w}_{exp} = [K(\mathbf{X}_{exp}, \mathbf{X}_{exp}) + \sigma^2_{n,exp}]^{-1}\mathbf{y}_{exp}$, with $\mathbf{X}_{exp}$ denoting the design matrix formed from experimental training inputs, $\mathbf{y}_{exp}$ denoting vector of experimental training outputs, and $\sigma^2_{n,exp}$ denoting the corresponding variance. Similar notations are defined for those of the simulated training data.

For the recursive prediction, the recursively predicted mean on the cross-sectional area $\widehat{A}(s)$, $(s = 1, \ldots, N)$, is computed as follows:

$$\widehat{A}(s) = \alpha\widehat{A}_{exp}(s) + (1-\alpha)\widehat{A}_{sim}(s) \tag{26}$$

where the computation of the recursive prediction of $\widehat{A}_{exp}$ and $\widehat{A}_{sim}$ follows a similar procedure as defined in (7) - (9) (noting that a fixed area-volume ratio γ is used to convert the predicted mean on melt-pool volume to that on the melt-pool cross-sectional area), using the experimental and simulated training sets, respectively. By mixture distribution, the variance $\sigma^2(\widehat{A})$ of the recursively predicted mean $\widehat{A}$ is then computed as:

$$\begin{aligned}\sigma^2(\widehat{A}(s)) = {} & \alpha\sigma^2(\widehat{A}_{exp}(s)) + (1-\alpha)\sigma^2(\widehat{A}_{sim}(s)) \\ & + \alpha\widehat{A}^2_{exp}(s) + (1-\alpha)\widehat{A}^2_{sim}(s) - \widehat{A}^2(s)\end{aligned} \tag{27}$$

To form the simulated training set $\mathcal{D}_{sim}$, same as in Sect. 5.1, 200 data points are randomly selected from the total of 8010 simulated data sets, and the rest 7810 data points are used for testing. To form the experimental training set $\mathcal{D}_{exp}$, 50 data points are randomly selected from the total of 64 experimental data sets, and the rest 14 data points are used for testing. Four choices of α are examined to evaluate the effect of the weighting parameter α on the model training and prediction: (i) $\alpha = 0.2$; (ii) $\alpha = 0.5$; (iii) $\alpha = 0.8$; and (iv) $\alpha = 1.0$. The first three cases correspond to a higher, equal, and lower confidence in the quality (fidelity) of the simulated data sets compared to the quality of the experimental data sets. In the fourth case, only the experimental data sets are used for training.

The hyperparameters are initialized as $\sigma^2_{l1} = \sigma^2_{l2} = \sigma^2_{l3} = \sigma^2_f = 1$ before training. For all choices of α, the noise variances for the simulated and experimental data are set as $\sigma^2_{n,sim} = 1 \times 10^{-4}$ and $\sigma^2_{n,exp} = 4 \times 10^{-4}$. Table 5 presents the hyperparameters obtained from training under the different values of α.

Figure 8 shows the scatter plots of the one-step predictions versus the ground truth values of the melt-pool cross-sectional area on the testing samples consisting of 7810 simulated data sets and 14 experimental data sets. The corresponding coefficients of determination R^2_{sim} and R^2_{exp} with respect to the simulated and experimental testing data are given in Table 6. With the increase of the weighting parameter α, R^2_{sim} decreases whereas R^2_{exp} increases, but overall the one-step predictions have reasonable agreement with the ground truth. For $\alpha = 1.0$, predictions made by the model trained with experimental data are tested with experimental data (14 data points) only. For one-step prediction, the model trained with the limited experimental data performs really well with respect to the testing data sets, with $R^2_{exp} = 0.9999$.

Table 5 Hyperparameters from training with the mix of simulated and experimental data sets

	σ^2_{l1}	σ^2_{l2}	σ^2_{l3}	σ^2_f
$\alpha = 0.2$	9.8066	9.3180	1.0237	0.2092
$\alpha = 0.5$	7.6949	8.6376	0.7231	0.1750
$\alpha = 0.8$	9.5031	9.2285	0.9781	0.2047
$\alpha = 1.0$	1.0	6.1424	0.2027	0.0768

Figure 9 shows the recursive prediction on melt-pool cross-sectional area with respect to the cumulative laser-travelled distance for the six-track, under different α values. With the increase of the α value from 0.2 to 0.8, the contribution of the simulated training sets to model prediction gets less whereas the influence of the experimental training sets gets higher, which renders the prediction to deviate away from the simulated ground truth but get closer to the experimental ground truth. The corresponding RMSE and average error rate of the recursive prediction with respect to the simulated or experimental ground truth are given in Table 6. Noting that sample variances exist in the experimental measurements, only the mean of the experimental measurements at each distance location is used in computing the RMSE and error rate with respect to the experimental ground truth. Consistent with the observations from Fig. 9, Table 6 shows that when α increases from 0.2 to 0.8, the recursive prediction with respect to the experimental testing samples has improved, with 36% reduction in RMSE and 23% reduction in the average error rate. For $\alpha = 1.0$, it appears that the number of experimental data sets used for training is not large enough to warrant a decent recursive prediction, and the resulting prediction has the worst agreement with the experimental data sets among all cases of α values. This indicates that when there is not sufficient experimental data available for training, it would help improve the model performance by training over a mix of experimental and simulated data sets, as the high-fidelity simulated data sets, although subject to errors, at least capture the right trend of the real data. Future work will evaluate experimentally how the resulting models under different α values would affect the model-based control performance.

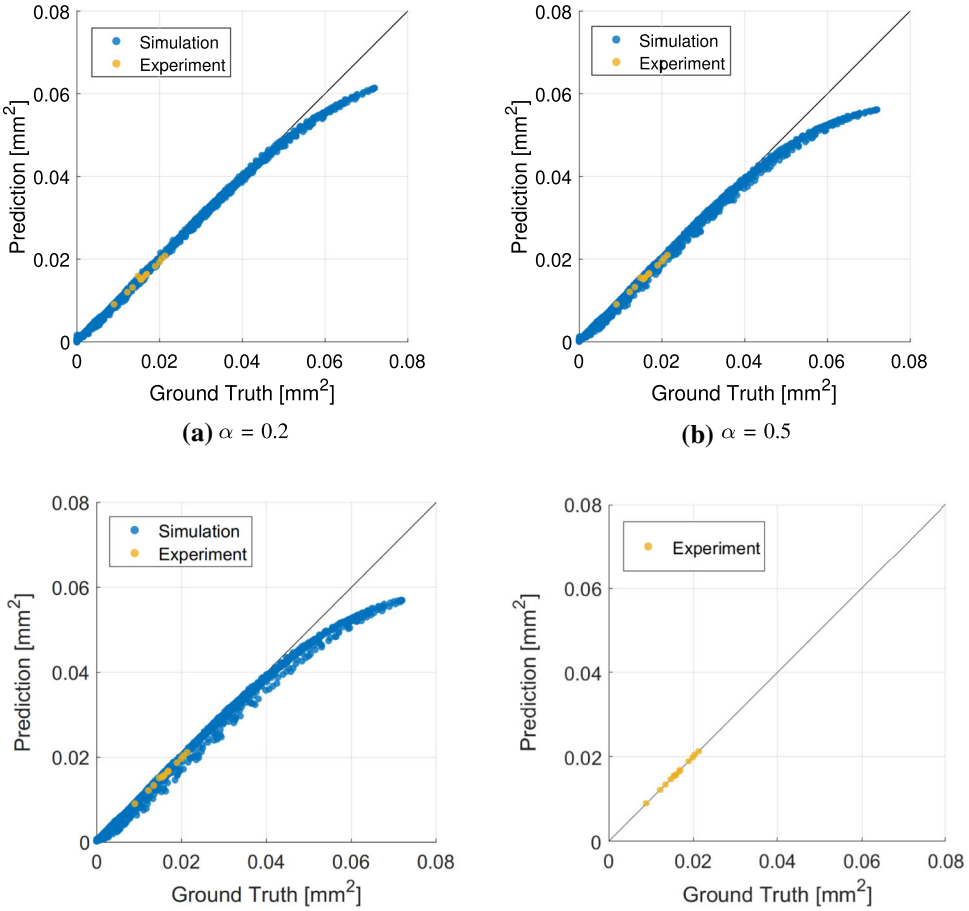

(a) $\alpha = 0.2$ **(b)** $\alpha = 0.5$ **(c)** $\alpha = 0.8$ **(d)** $\alpha = 1.0$

Fig. 8 Scatter plots of one-step prediction versus the ground truth of melt-pool cross-sectional area on simulated and experimental testing samples. For $\alpha = 1$, only experimental data are used for model training and thus comparison with respect to only experimental ground truth is shown

Conclusions

This paper considered modeling and control of melt-pool dynamics for multi-tracks built with L-PBF AM processes. First a physics-informed Gaussian process regression (GPR) model was developed to model the dynamic evolution of melt-pool size along the laser scanning distance during the build process. Then, based on the predictions of the GPR model, a (sub)optimal control of laser power, derived using a projected gradient descent algorithm, was applied to regulate the melt-pool size to a constant reference value. The proposed GPR modeling was demonstrated using pure simulated data sets, a mix of simulated and experimental data sets, or pure experimental data sets. The GPR-model-based control was evaluated through a commercial finite-element based AM software. Simulation studies of multi-track laser processing demonstrated good modeling and control performance. Results from this study indicated that the proposed GPR machine-learning modeling and control could be a promising tool in regulating the melt-pool size during the build process, and thus could potentially be used to improve build quality for components fabricated with L-PBF AM processes. This study also shows that when there is not sufficient experimental data available for model training, it would help improve the model performance by training over a mixed set of experimental and high-fidelity simulated data sets. Future work will

Table 6 Prediction performance under different weighting parameter α

	One-step Prediction		Recursive Prediction			
	R^2_{sim}	R^2_{exp}	RMSE$_{sim}$ (mm^2)	e_{sim}%	RMSE$_{exp}$ (mm^2)	e_{exp}%
$\alpha = 0.2$	0.9969	0.9687	0.0027	10.35	0.0076	43.09
$\alpha = 0.5$	0.9916	0.9867	0.0038	10.31	0.0056	37.00
$\alpha = 0.8$	0.9906	0.9971	0.0060	14.65	0.0049	33.25
$\alpha = 1.0$	–	0.9999	–	–	0.0095	87.74

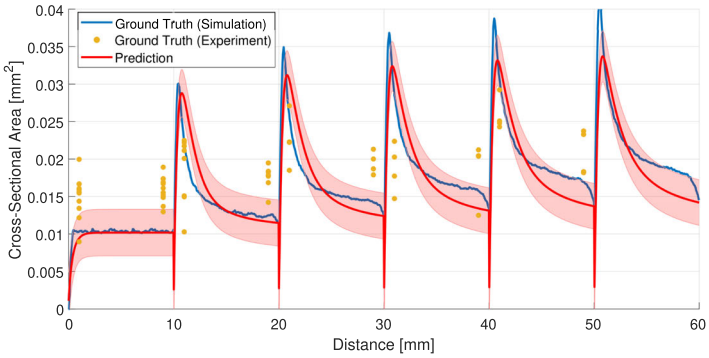

(a) $\alpha = 0.2$

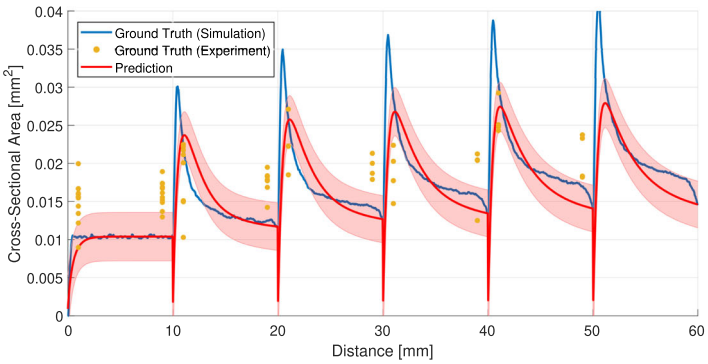

(b) $\alpha = 0.5$

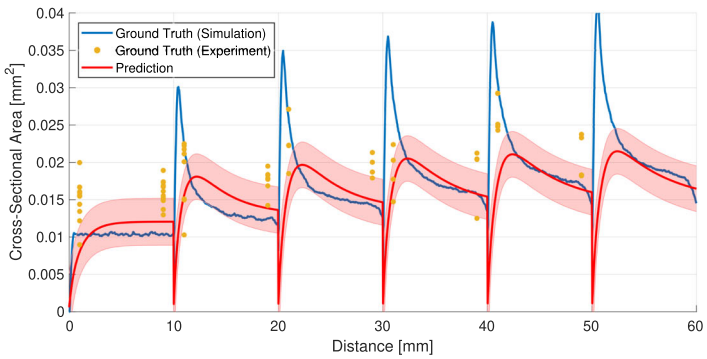

(c) $\alpha = 0.8$

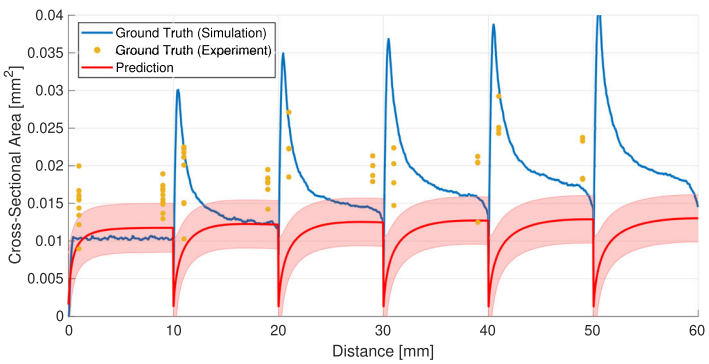

(d) $\alpha = 1.0$

Fig. 9 Recursive prediction on melt-pool cross-sectional area with respect to the (cumulative laser-travelled) distance for the six-track; $L = 10$ mm, laser power = 250 W, and scan speed = 600 mm/s. The shaded area represents 2σ of the recursively predicted mean (red solid line)

extend the proposed model to include a more extensive set of process parameters. In addition, future work will include model prediction of other melt-pool geometric variables such as melt-pool width or depth.

Declarations

Funding This project was financed in part by a grant from the Commonwealth of Pennsylvania, Department of Community and Economic Development. Any opinions, findings, conclusions or recommendations expressed herein are those of the authors and do not reflect the views of the Commonwealth of Pennsylvania. This paper was also supported in part by Penn State ICDS Seed Grant and NSF grant 2015930.

Conflict of interest The authors have no conflict of interest to declare that are relevant to the content of this article.

A. Computation of initial temperature

Consider the multi-track shown in Fig. 1. Define a fixed coordinate system with the origin at the starting point of the first track, x-axis pointing to the laser scanning direction of the first track, and y-axis pointing to the direction where subsequent tracks will be scanned. Without loss of generality, consider that the laser is melting the ith track and it is going to scan a point with coordinates $\mathbf{p} = [x; y]$ on this track. Noting that a multi-track single-layer is considered here, thus 2-dim coordinates are sufficient to describe any point in the build plane.

When the laser scans the first track ($i = 1$), the initial temperature T_{init} equals to the ambient temperature T_a, i.e., $T_{init} = T_a$. When $i > 1$, to account for the temperature contribution of each past track j ($j = 1, \ldots, i-1$) to the point $\mathbf{p}$, a virtual heat source j is assigned to replace the original laser heat source as soon as it finishes scanning track j. The virtual heat source continues to travel along the same direction at the same scanning speed v_j and with the same power value (Q_j) as the physical laser heat source at the end of track j. A pair of virtual heat source and heat sink could be defined to better characterize the temperature cooling after the physical laser heat source finishes scanning the track j, but the temperature difference between using a pair of virtual heat source/sink and using a single virtual heat source is negligible in this study, and hence the latter is used for simplicity.

Let $\mathbf{p}_j = [x_j; y_j]$ denote the coordinates of the virtual heat source j. Computation of such coordinates could easily account for the build plan and inter-hatch dwell time (including skywriting time and any additional dwell), during which the virtual heat source keeps traveling. Let q_j denote the net power of the virtual heat source of track j, which equals to the product of laser power Q_j and the laser absorption efficiency. Then the initial temperature at point $\mathbf{p}$ on the ith track is computed as the summation of the ambient temperature and temperature contributions from all virtual heat sources j, $j = 1, \ldots, i-1$, given as follows:

$$T_{init}(\mathbf{p}) = T_a + \sum_{j=1}^{i-1} \frac{q_j}{2\pi k \|\mathbf{p} - \mathbf{p}_j\|_2} e^{-\frac{v_j(w_j + \|\mathbf{p} - \mathbf{p}_j\|_2)}{2a}} \tag{28}$$

with each term in the summation representing the Rosenthal's solution (Rosenthal 1946) due to a virtual heat source j. In (28), $w_j = x - x_j$, $\|\cdot\|_2$ denotes the 2-norm. Constant values of the thermal conductivity k and thermal diffusivity a for Inconel 625 listed in Table 1 are used here, in contrast to temperature-dependent material properties used in FEA. For the ith track, to compute $T_{init}(s)$ using (28), the coordinates $\mathbf{p} = [x; y]$ can be easily computed as follows: $x = s$ for an odd-number track and $x = L - s$ for an even-number track; $y = (i-1) \cdot h$ with h denoting the hatch space. Our prior study showed that this analytical computation has a good agreement, to a certain extent, with FEA simulations (Li et al. 2017).

B. Computation of GPR estimated melt-pool volumes and partial derivatives

Consider that the design matrix $\mathbf{X}$ consists of n training data, i.e., $\mathbf{X} = [\mathbf{x}_1, \cdots, \mathbf{x}_j, \cdots, \mathbf{x}_n]$ where each training data $\mathbf{x}_j = [V_j, Q_j, T_{init,j}]^T$ consists of three elements $\mathbf{x}_j(1) = V_j$, $\mathbf{x}_j(2) = Q_j$, and $\mathbf{x}_j(3) = T_{init,j}$. By the squared exponential covariance function in (10), the matrix $K(\widehat{\boldsymbol{\xi}}(s), \mathbf{X})$ of dimension $1 \times n$ is given in (29) below. For $\mathbf{w} = [w_1, \cdots, w_j, \cdots, w_n]^T$, the estimated states $\widehat{V}(s+1)$ in (7) - (9) and their partial derivatives are given in (30) - (32) below.

$$K(\widehat{\boldsymbol{\xi}}(s), \mathbf{X}) = \sigma_f^2 \cdot \begin{pmatrix} e^{-\frac{1}{2}[(\widehat{V}(s)-\mathbf{x}_1(1))^2/\sigma_{l1}^2 + (Q(s)-\mathbf{x}_1(2))^2/\sigma_{l2}^2 + (T_{init}(s)-\mathbf{x}_1(3))^2/\sigma_{l3}^2]} \\ \vdots \\ e^{-\frac{1}{2}[(\widehat{V}(s)-\mathbf{x}_j(1))^2/\sigma_{l1}^2 + (Q(s)-\mathbf{x}_j(2))^2/\sigma_{l2}^2 + (T_{init}(s)-\mathbf{x}_j(3))^2/\sigma_{l3}^2]} \\ \vdots \\ e^{-\frac{1}{2}[(\widehat{V}(s)-\mathbf{x}_n(1))^2/\sigma_{l1}^2 + (Q(s)-\mathbf{x}_n(2))^2/\sigma_{l2}^2 + (T_{init}(s)-\mathbf{x}_n(3))^2/\sigma_{l3}^2]} \end{pmatrix}^T \tag{29}$$

$$\widehat{V}(s+1) = \sum_{j=1}^{n} w_j \sigma_f^2 \cdot e^{-\frac{1}{2}[(\widehat{V}(s)-\mathbf{x}_j(1))^2/\sigma_{l1}^2 + (Q(s)-\mathbf{x}_j(2))^2/\sigma_{l2}^2 + (T_{init}(s)-\mathbf{x}_j(3))^2/\sigma_{l3}^2]} \tag{30}$$

$$\frac{\partial \widehat{V}(s+1)}{\partial \widehat{V}(s)} = -\sum_{j=1}^{n} w_j \sigma_f^2 \cdot \frac{\widehat{V}(s) - \mathbf{x}_j(1)}{\sigma_{l1}^2} \cdot e^{-\frac{1}{2}[(\widehat{V}(s)-\mathbf{x}_j(1))^2/\sigma_{l1}^2 + (Q(s)-\mathbf{x}_j(2))^2/\sigma_{l2}^2 + (T_{init}(s)-\mathbf{x}_j(3))^2/\sigma_{l3}^2]} \tag{31}$$

$$\frac{\partial \widehat{V}(s+1)}{\partial Q(s)} = -\sum_{j=1}^{n} w_j \sigma_f^2 \cdot \frac{Q(s) - \mathbf{x}_j(2)}{\sigma_{l2}^2} \cdot e^{-\frac{1}{2}[(\widehat{V}(s)-\mathbf{x}_j(1))^2/\sigma_{l1}^2 + (Q(s)-\mathbf{x}_j(2))^2/\sigma_{l2}^2 + (T_{init}(s)-\mathbf{x}_j(3))^2/\sigma_{l3}^2]} \tag{32}$$

References

Jiang, J., Newman, S. T., & Zhong, R. Y. (2021). A review of multiple degrees of freedom for additive manufacturing machines. *Inter-*

national Journal of Computer Integrated Manufacturing, *34*(2), 195–211.

Levy, G. N., Schindel, R., & Kruth, J.-P. (2003). Rapid manufacturing and rapid tooling with layer manufacturing (lm) technologies, state of the art and future perspectives. *CIRP Annals*, *52*(2), 589–609.

Kruth, J.-P., Levy, G., Klocke, F., & Childs, T. (2007). Consolidation phenomena in laser and powder-bed based layered manufacturing. *CIRP Annals*, *56*(2), 730–759.

Druzgalski, C., Ashby, A., Guss, G., King, W., Roehling, T., & Matthews, M. (2020). Process optimization of complex geometries using feed forward control for laser powder bed fusion additive manufacturing. *Additive Manufacturing*, *2*, 101169.

Dilip, J., Zhang, S., Teng, C., Zeng, K., Robinson, C., & Pal, D. (2017). Influence of processing parameters on the evolution of melt pool, porosity, and microstructures in Ti-6Al-4V alloy parts fabricated by selective laser melting. *Progress in Additive Manufacturing*, *2*(3), 157–167.

Kumar, P., Farah, J., Akram, J., Teng, C., Ginn, J., & Misra, M. (2019). Influence of laser processing parameters on porosity in inconel 718 during additive manufacturing. *The International Journal of Advanced Manufacturing Technology*, *103*(1–4), 1497–1507.

Ning, J., Sievers, D. E., Garmestani, H., & Liang, S. Y. (2020). Analytical modeling of part porosity in metal additive manufacturing. *International Journal of Mechanical Sciences*, *172*, 105428.

Craeghs, T., Bechmann, F., Berumen, S., & Kruth, J.-P. (2010). Feedback control of layerwise laser melting using optical sensors. *Physics Procedia*, *5*, 505–514.

Wang, D., Jiang, T., & Chen, X. (2019). Control-oriented modeling and repetitive control in in-layer and cross-layer thermal interactions in selective laser sintering. In *Proceedings of the ASME dynamic systems and control conference*.

Wang, Q. (2019). A control-oriented model for melt-pool volume in laser powder bed fusion additive manufacturing. In: *Dynamic Systems and Control Conference, Vol. 59148, American Society of Mechanical Engineers*, p. V001T10A002.

Wang, Q., Michaleris, P., Nassar, A. R., Irwin, J. E., Ren, Y., & Stutzman, C. B. (2020). Model-based feedforward control of laser powder bed fusion additive manufacturing. *Additive Manufacturing*, *31*, 110.

Devesse, W., De Baere, D., & Guillaume, P. (2014). Design of a model-based controller with temperature feedback for laser cladding. *Physics Procedia*, *56*, 211–219.

Devesse, W., De Baere, D., Hinderdael, M., & Guillaume, P. (2016). Hardware-in-the-loop control of additive manufacturing processes using temperature feedback. *Journal of Laser Applications*, *28*(2), 022302.

Dillkötter, D., & Mönnigmann, M. (2019). Design of a model based feedforward controller for additive manufacturing by laser metal deposition. In *2019 18th European control conference (ECC)* (pp. 3842–3847), IEEE.

Gobert, C., Reutzel, E. W., Petrich, J., Nassar, A. R., & Phoha, S. (2018). Application of supervised machine learning for defect detection during metallic powder bed fusion additive manufacturing using high resolution imaging. *Additive Manufacturing*, *21*, 517–528.

Yuan, B., Guss, G. M., Wilson, A. C., Hau-Riege, S. P., DePond, P. J., & McMains, S. (2018). Machine-learning-based monitoring of laser powder bed fusion. *Advanced Materials Technologies*, *3*(12), 1800136.

Yang, Z., Lu, Y., Yeung, H., & Krishnamurty, S. (2019). Investigation of deep learning for real-time melt pool classification in additive manufacturing. In *2019 IEEE 15th international conference on automation science and engineering (CASE)* (pp. 640–647), IEEE.

Scime, L., & Beuth, J. (2018). A multi-scale convolutional neural network for autonomous anomaly detection and classification in a laser powder bed fusion additive manufacturing process. *Additive Manufacturing*, *24*, 273–286.

Scime, L., & Beuth, J. (2019). Using machine learning to identify in-situ melt pool signatures indicative of flaw formation in a laser powder bed fusion additive manufacturing process. *Additive Manufacturing*, *25*, 151–165.

Gaikwad, A., Yavari, R., Montazeri, M., Cole, K., Bian, L., & Rao, P. (2020). Toward the digital twin of additive manufacturing: Integrating thermal simulations, sensing, and analytics to detect process faults. *IISE Transactions,* 1–14.

Aminzadeh, M., & Kurfess, T. R. (2019). Online quality inspection using bayesian classification in powder-bed additive manufacturing from high-resolution visual camera images. *Journal of Intelligent Manufacturing*, *30*(6), 2505–2523.

Zhang, Y., Hong, G. S., Ye, D., Zhu, K., & Fuh, J. Y. (2018). Extraction and evaluation of melt pool, plume and spatter information for powder-bed fusion am process monitoring. *Materials & Design*, *156*, 458–469.

Razvi, S. S., Feng, S., Narayanan, A., Lee, Y.-T. T., & Witherell, P. (2019). A review of machine learning applications in additive manufacturing. In *ASME 2019 international design engineering technical conferences and computers and information in engineering conference*. American Society of Mechanical Engineers Digital Collection.

Meng, L., McWilliams, B., Jarosinski, W., Park, H.-Y., Jung, Y.-G., Lee, J., & Zhang, J. (2020). Machine learning in additive manufacturing: A review. *JOM,* 1–15.

Lu, Z., Li, D., Lu, B., Zhang, A., Zhu, G., & Pi, G. (2010). The prediction of the building precision in the laser engineered net shaping process using advanced networks. *Optics and Lasers in Engineering*, *48*(5), 519–525.

Mozaffar, M., Paul, A., Al-Bahrani, R., Wolff, S., Choudhary, A., & Agrawal, A. (2018). Data-driven prediction of the high-dimensional thermal history in directed energy deposition processes via recurrent neural networks. *Manufacturing Letters*, *18*, 35–39.

Ren, K., Chew, Y., Zhang, Y., Fuh, J., & Bi, G. (2020). Thermal field prediction for laser scanning paths in laser aided additive manufacturing by physics-based machine learning. *Computer Methods in Applied Mechanics and Engineering*, *362*, 112734.

Rong-Ji, W., Xin-Hua, L., Qing-Ding, W., & Lingling, W. (2009). Optimizing process parameters for selective laser sintering based on neural network and genetic algorithm. *The International Journal of Advanced Manufacturing Technology*, *42*(11–12), 1035–1042.

Zhang, W., Mehta, A., Desai, P. S., & Higgs, C. (2017). Machine learning enabled powder spreading process map for metal additive manufacturing (am). In *International Solid Free Form Fabric Symposium Austin* (pp. 1235–1249).

Kappes, B., Moorthy, S., Drake, D., Geerlings, H., & Stebner, A. (2018). Machine learning to optimize additive manufacturing parameters for laser powder bed fusion of inconel 718. In *Proceedings of the 9th international symposium on superalloy 718 & derivatives: Energy, aerospace, and industrial applications* (pp. 595–610), Springer.

Yang, Z., Eddy, D., Krishnamurty, S., Grosse, I., Denno, P., & Witherell, P. W. (2018). Dynamic metamodeling for predictive analytics in advanced manufacturing. *Smart and Sustainable Manufacturing Systems*, *2*, 18–39.

Tapia, G., Khairallah, S., Matthews, M., King, W. E., & Elwany, A. (2018). Gaussian process-based surrogate modeling framework for process planning in laser powder-bed fusion additive manufacturing of 316l stainless steel. *The International Journal of Advanced Manufacturing Technology*, *94*(9–12), 3591–3603.

Gaikwad, A., Giera, B., Guss, G. M., Forien, J.-B., Matthews, M. J., & Rao, P. (2020). Heterogeneous sensing and scientific machine learning for quality assurance in laser powder bed fusion-a single-track study. *Additive Manufacturing*, *3*, 101659.

Meng, L., & Zhang, J. (2020). Process design of laser powder bed fusion of stainless steel using a gaussian process-based machine learning model. *JOM*, *72*(1), 420–428.

Khairallah, S. A., Anderson, A. T., Rubenchik, A., & King, W. E. (2016). Laser powder-bed fusion additive manufacturing: Physics of complex melt flow and formation mechanisms of pores, spatter, and denudation zones. *Acta Materialia*, *108*, 36–45.

Ren, Y., Wang, Q., & Michaleris, P. (2019). Machine-learning based thermal-geometric predictive modeling of laser powder bed fusion additive manufacturing. *Proceedings of the ASME Dynamic Systems and Control Conference,* 390–397.

Rasmussen, C. E., & Williams, C. K. I. (2006). *Gaussian processes for machine learning*. Cambridge: The MIT Press.

Beckers, T., Kulić, D., & Hirche, S. (2019). Stable Gaussian process based tracking control of Euler-Lagrange systems. *Automatica*, *103*, 63.

Baturynska, I., Semeniuta, O., & Martinsen, K. (2018). Optimization of process parameters for powder bed fusion additive manufacturing by combination of machine learning and finite element method: A conceptual framework. *Procedia CIRP*, *67*, 227–232.

Ren, Y., & Wang, Q. (2020). Physics-informed gaussian process based optimal control of laser powder bed fusion. In *ASME 2020 dynamic systems and control conference*.

Wang, Q., Li, J., Nassar, A. R., Reutzel, E. W., & Mitchell, W. F. (2021). Model-based feedforward control of part height in directed energy deposition. *Materials*, *14*(2), 337.

Ghosh, S., Ma, L., Levine, L. E., Ricker, R. E., Stoudt, M. R., & Heigel, J. C. (2018). Single-track melt-pool measurements and microstructures in inconel 625. *JOM*, *70*(6), 1011–1016.

Heigel, J. C., & Lane, B. M. (2018). Measurement of the melt pool length during single scan tracks in a commercial laser powder bed fusion process. *Journal of Manufacturing Science and Engineering*, *140*(5), 051012.

Rosenthal, D. (1946). The theory of moving sources of heat and its application to metal treatment. *Transactions of the American Society of Mechanical Engineers*, *43*, 849–866.

Li, J., Wang, Q., Michaleris, P., Reutzel, E. W., & Nassar, A. R. (2017). An analytical computation of temperature field evolved in directed energy deposition. *Journal of Manufacturing Science and Engineering*, *139*, 56.